IJMMM
International Journal of
Minerals, Metallurgy and Materials
矿物冶金与材料学报（英文版）

Improving creep strength of the fine-grained heat-affected zone of novel 9Cr martensitic heat-resistant steel via modified thermo-mechanical treatment

Jingwen Zhang, Liming Yu, Yongchang Liu, Ran Ding, Chenxi Liu, Zongqing Ma, Huijun Li, Qiuzhi Gao, and Hui Wang

Cite this article as:
Jingwen Zhang, Liming Yu, Yongchang Liu, Ran Ding, Chenxi Liu, Zongqing Ma, Huijun Li, Qiuzhi Gao, and Hui Wang, Improving creep strength of the fine-grained heat-affected zone of novel 9Cr martensitic heat-resistant steel via modified thermo-mechanical treatment, *Int. J. Miner. Metall. Mater.*, 31(2024), No. 5, pp. 1037-1047. https://doi.org/10.1007/s12613-023-2760-0

View the article online at SpringerLink or IJMMM Webpage.

Articles you may be interested in

Jun-jun Yan, Xue-fei Huang, and Wei-gang Huang, High-temperature oxidation behavior of 9Cr5Si3Al ferritic heat-resistant steel, *Int. J. Miner. Metall. Mater.*, 27(2020), No. 9, pp. 1244-1250. https://doi.org/10.1007/s12613-019-1961-z

Hassan Kazempour-Liasi, Mohammad Tajally, and Hassan Abdollah-Pour, Liquation cracking in the heat-affected zone of IN939 superalloy tungsten inert gas weldments, *Int. J. Miner. Metall. Mater.*, 27(2020), No. 6, pp. 764-773. https://doi.org/10.1007/s12613-019-1954-y

Jin-hua Zhou, Yong-feng Shen, and Nan Jia, Strengthening mechanisms of reduced activation ferritic/martensitic steels: A review, *Int. J. Miner. Metall. Mater.*, 28(2021), No. 3, pp. 335-348. https://doi.org/10.1007/s12613-020-2121-1

Arian Ghandi, Morteza Shamanian, Mohamad Reza Salmani, and Jalal Kangazian, Improvement of the microstructural features and mechanical properties of advanced high-strength steel DP590 welds, *Int. J. Miner. Metall. Mater.*, 28(2021), No. 6, pp. 1022-1029. https://doi.org/10.1007/s12613-020-2117-x

Yu Shao, Li-ming Yu, Yong-chang Liu, Zong-qing Ma, Hui-jun Li, and Jie-feng Wu, Hot deformation behaviors of a 9Cr oxide dispersion-strengthened steel and its microstructure characterization, *Int. J. Miner. Metall. Mater.*, 26(2019), No. 5, pp. 597-610. https://doi.org/10.1007/s12613-019-1768-y

V.T. Gaikwad, M.K. Mishra, V.D. Hiwarkar, and R.K.P. Singh, Microstructure and mechanical properties of friction welded carbon steel (EN24) and nickel-based superalloy (IN718), *Int. J. Miner. Metall. Mater.*, 28(2021), No. 1, pp. 111-119. https://doi.org/10.1007/s12613-020-2008-1

IJMMM WeChat

QQ author group

INTERNATIONAL JOURNAL OF
Minerals, Metallurgy and Materials

Volume 31, Number 5, May 2024
Page 1037

Research Article https://doi.org/10.1007/s12613-023-2760-0

Improving creep strength of the fine-grained heat-affected zone of novel 9Cr martensitic heat-resistant steel via modified thermo-mechanical treatment

Jingwen Zhang[1)], *Liming Yu*[1),✉], *Yongchang Liu*[1),✉], *Ran Ding*[1)], *Chenxi Liu*[1)], *Zongqing Ma*[1)], *Huijun Li*[1)], *Qiuzhi Gao*[2)], and *Hui Wang*[3)]

1) State Key Lab of Hydraulic Engineering Simulation and Safety, Tianjin Key Lab of Composite and Functional Materials, Tianjin University, Tianjin 300072, China
2) School of Resources and Materials, Northeastern University at Qinhuangdao, Qinhuangdao 066004, China
3) School of Mechanical Engineering, Chengdu University, Chengdu 610106, China

(Received: 14 July 2023; revised: 22 September 2023; accepted: 9 October 2023)

Abstract: The infamous type IV failure within the fine-grained heat-affected zone (FGHAZ) in G115 steel weldments seriously threatens the safe operation of ultra-supercritical (USC) power plants. In this work, the traditional thermo-mechanical treatment was modified via the replacement of hot-rolling with cold rolling, i.e., normalizing, cold rolling, and tempering (NCT), which was developed to improve the creep strength of the FGHAZ in G115 steel weldments. The NCT treatment effectively promoted the dissolution of preformed $M_{23}C_6$ particles and relieved the boundary segregation of C and Cr during welding thermal cycling, which accelerated the dispersed reprecipitation of $M_{23}C_6$ particles within the fresh reaustenitized grains during post-weld heat treatment. In addition, the precipitation of Cu-rich phases and MX particles was promoted evidently due to the deformation-induced dislocations. As a result, the interacting actions between precipitates, dislocations, and boundaries during creep were reinforced considerably. Following this strategy, the creep rupture life of the FGHAZ in G115 steel weldments can be prolonged by 18.6%, which can further push the application of G115 steel in USC power plants.

Keywords: G115 steel; fine-grained heat-affected zone; creep strength; element segregation; nano-sized precipitates

1. Introduction

The urgent need to reduce energy consumption and protect the environment will promote next-grade ultra-supercritical (USC) power plants to operate at 650°C with a stress level of 35 MPa, which will trigger the development of advanced structural materials with superior creep strength and oxidation resistance [1–5]. Based on this background, a novel martensitic heat-resistant G115 steel with an alloying composition of 9Cr–3W–3Co–1Cu–VNb has been designed based on the element-selective reinforcement theory [6–7]. Compared with traditional P91 (9Cr–1Mo–VNb) or P92 (9Cr–1.8W0.5Mo–VNb) steels, G115 steel is added with more W and Co to reinforce solid solution strengthening and precipitation strengthening through the suppressed coarsening of $M_{23}C_6$ carbides [8]. Moreover, an increased content of B in combination with a balanced content of N is optimized to promote the precipitation of fine MX carbonitrides [9]. In addition, the addition of a minor amount of Cu (~1wt%) results in the formation of Cu-rich phases, which can provide an additional precipitation strengthening effect [10]. The excellent creep strength of G115 steel can be ascribed to the reinforced interactions among precipitates, dislocations, and boundaries [11–12].

As large components in USC power plants must be manufactured by fusion welding technologies, the G115 steel must undergo the welding process [6,13–14]. In our previous investigation [15], the fabricated G115 welded joint exhibited inferior creep strength compared with the base material due to type IV cracking within the fine-grained heat-affected zone (FGHAZ) during the long-term creep test, and this result could be ascribed to the coarsening of $M_{23}C_6$ particles and the rapid recovery of dislocations. Pandey *et al.* [16] also proved that some $M_{23}C_6$ carbides that were retained during welding thermal cycling in the FGHAZ could grow further during the subsequent post-weld heat treatment (PWHT) and act as preferred nucleation sites for creep cavities owing to their incompatible deformation ability with the matrix. Additionally, Wang *et al.* [17] observed that the Cr or C originating from partially dissolved $M_{23}C_6$ carbides were prone to segregate along the prior austenite grain boundaries in the FGHAZ during the welding process due to their rapid cooling rate, which could lead to the scarce precipitation of fresh $M_{23}C_6$ carbides within the newly formed reaustenitized grains during PWHT, thus weakening the sub-boundary strengthening effect. Hence, the creep strength of FGHAZ can be im-

---

✉ Corresponding authors: Liming Yu E-mail: lmyu@tju.edu.cn; Yongchang Liu E-mail: ycliu@tju.edu.cn

proved through the dissolution of the preformed $M_{23}C_6$ carbides and the relief or elimination of Cr or C segregation along boundaries during the welding process. In addition, the nano-sized MX carbonitrides and Cu-rich phases play a crucial role in the improved creep strength of G115 steel [7,10,18].

Recently, thermo-mechanical treatment (TMT) has gained growing interest owing to its outstanding contribution to the improved creep strength of precipitate-strengthened martensitic heat-resistant steels [19–21]. TMT induces complex dislocation structures within the matrix, which can promote the precipitation of strengthening particles. According to Sakthivel *et al.* [22], a finer lath structure with higher dislocation density and uniform distribution of $M_{23}C_6$ and MX particles could be obtained in 9Cr–1Mo steel after TMT, which effectively reduced the recovery rate of dislocation structure and delayed lath coarsening. Vivas *et al.* [23] also stated that high normalizing temperature combined with deformation during TMT could accelerate the precipitation of MX particles in G91 steels and enhance the creep strength considerably. Sakthivel *et al.* [24] investigated the effect of TMT on the creep strength of P92 steel and indicated that the homogeneously distributed precipitates could reduce the creep rate by pinning the boundary migrations and blocking dislocation motions. TMT has exhibited promising applications in the improvement of the creep strength of martensitic heat-resistant steels, but its feasibility for application in weldments remains poorly understood. Meanwhile, TMT is sensitive to deformation temperature and rolling rate [25–26]. The enhanced transformation kinetics of γ to α results in the formation of some α-ferrite grains after TMT [27]. In addition, partial dislocation recovery and boundary migration at high aging temperatures result in the additional formation of subgrains with a low hardness, which can deteriorate creep strength [28].

Industrial heat treatments for G115 steel include normalizing and tempering (NT), which guarantees the optimized combination of creep strength and impact toughness [29–30]. However, the infamous type IV failure within the FGHAZ limits the wide application of G115 steel in USC power plants. Hence, a modified TMT involving normalizing, cold rolling, and tempering (NCT) has been proposed to improve the creep strength of the FGHAZ in G115 steel welded joints, and it is expected to solve element segregation and the uneven distribution of precipitates. Moreover, clarifications were provided for the evolution of grain structure and distribution of strengthening particles during thermal cycles and PWHT. Investigations were also conducted to determine the mechanical properties, creep behaviors, and the corresponding damage mechanism. The obtained experimental results can provide important technological data and theoretical basis for the industrial applications of G115 steel.

2. Experimental

2.1. Materials

G115 steel, whose main chemical compositions are provided in Table 1, was selected as the experimental material. The raw materials were melted in a vacuum induction furnace and casted into an ingot, which was forged into slabs measuring 100 mm × 100 mm × 20 mm.

2.2. NT and NCT treatments and FGHAZ simulation

Fig. 1(a) displays the schematics of the industrial NT treatment and the developed NCT treatment for G115 steel. In the NT treatment, the steel was first normalized at 1100°C for 60 min, and then cooled to room temperature by air cooling. After that, the normalized steel was tempered at 780°C for 180 min, and followed by air cooling. In the NCT treatment, the normalized steel was cold-rolled with 20% reduction in thickness to endow the matrix with higher dislocation density, and then tempered at 780°C for 60 min.

According to our previous investigations [15,31], the width of FGHAZ in the actual G115 steel welded joints is only 0.5–1 mm, which is difficult to precisely extract this zone, and then investigate its creep properties. Therefore, a Gleeble-3800 thermomechanical simulator was used for the reproduction of FGHAZ specimens for NT and NCT steels [28,32]. Fig. 1(b) reveals the dilatometric curves obtained from the Gleeble simulation, which can be used to measure the austenite phase transition temperatures Ac_1 and Ac_3. The NT steel had Ac_1 and Ac_3 temperatures of approximately 911°C and 969°C, respectively, and those of the NCT steel were around 898°C and 965°C.

Fig. 1(c) presents the thermal cycle histories of FGHAZ simulation and PWHT of NT and NCT steels. Given the thermal sensitivity of G115 steel, preheating was conducted at 200°C for 20 min before welding to avoid the formation of cold cracks [31]. During the actual welding thermal cycling, the FGHAZ consistently experienced a peak temperature above or close to Ac_3 [17,33]. Hence, the peak temperature and holding time for the FGHAZ simulation of both steels were set as 1050°C and 4 s, respectively. During the heating process in actual welding, the FGHAZ experienced a rapid heating rate due to its proximity to the fusion line [34]. Hence, in this work, the heating rate was set as 100°C/s, which is close to that of the actual welding process. Meanwhile, during the cooling process in actual welding, repeated heating of the FGHAZ occurred due to the subsequent deposition process, which resulted in a gradually decreased cooling rate. Hence, the cooling cycles in this work were programmed to follow the exponential equation [33,35]:

$$T = T_{\mathrm{p}} \times \exp^{\left(\frac{-0.47t}{\Delta t}\right)} \tag{1}$$

where T is the instantaneous temperature (°C), T_{p} refers to the

Table 1. Main chemical compositions of the as-received G115 steel wt%

C	Cr	W	Co	Si	Mn	V	Nb	N	B	Cu
0.074	9.15	2.77	2.91	0.32	0.50	0.19	0.056	0.015	0.0074	1.16

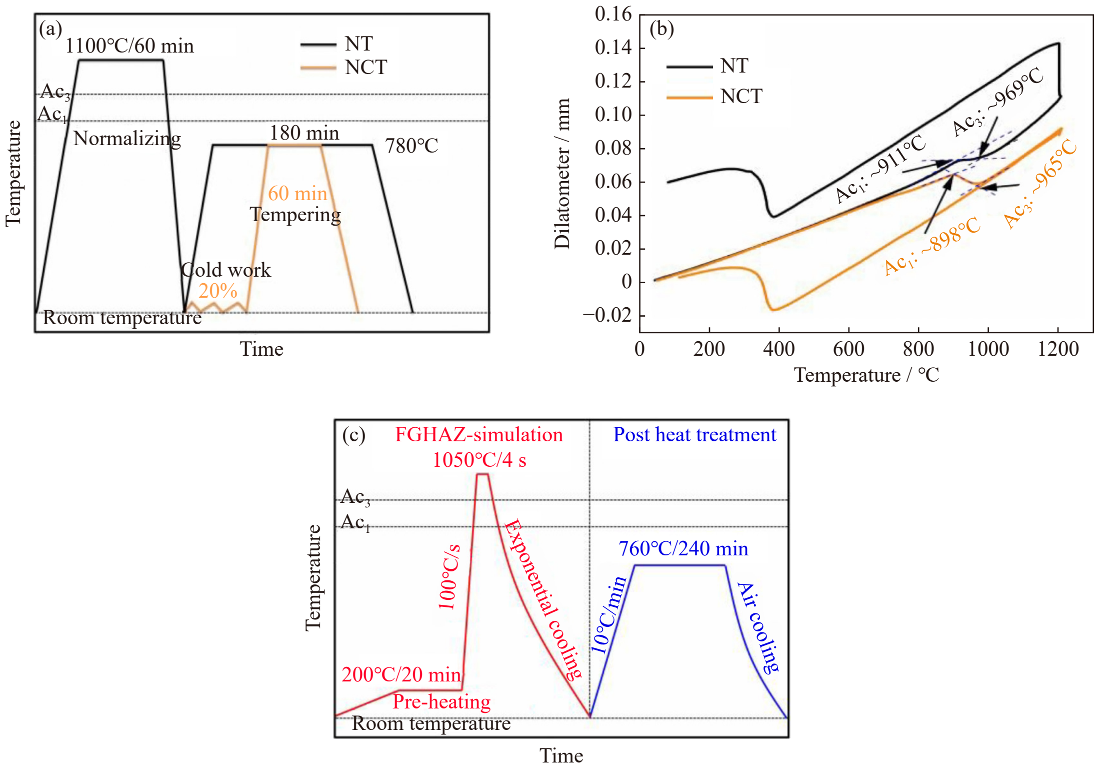

Fig. 1. (a) NT and NCT treatments of G115 steel, (b) dilatometric curves obtained from Gleeble simulation and measurement of Ac_1 and Ac_3 temperatures, and (c) thermal cycle histories of NT-FG and NCT-FG steels and the corresponding post heat treatments.

peak temperature (°C), t denotes the time interval (s), and Δt indicates the cooling period from 800 to 500°C, which was set as ~30 s.

In the case of the actual welded joints, PWHTs are necessary to eliminate the heterogeneity of microstructure and mechanical properties across the welded section [36–37]. Therefore, all the FGHAZ-simulation specimens were post heat-treated at 760°C for 240 min and air-cooled. For the purposes of discussion, the FGHAZ-simulation specimens of NT and NCT steels are hereafter referred to as NT-FG and NCT-FG steels, respectively.

2.3. Tensile, Charpy impact and creep tests

Fig. 2(a) and (b) displays the location of the FGHAZ in G115 steel weldments and the actual NT-FG and NCT-FG steels. The homogeneous FGHAZ obtained from the simulation had a width of ~10 mm. To guarantee the fracture occur within the FGHAZ during tensile and creep tests, specially designed testing specimens were used.

The sub-sized specimens (gauge length: 15 mm and thickness: 1 mm) were subjected to uniaxial tensile tests at a strain rate of $1 \times 10^{-3}\ s^{-1}$ at 25°C. Meanwhile, a narrow portion with a length of 8 mm and a width of 1 mm was machined within the FGHAZ (Fig. 2(c)). Charpy impact tests were conducted at 25°C on the sub-sized V-notch impact specimens (5 mm × 10 mm × 55 mm), and the notch was machined at the middle of FGHAZ (Fig. 2(d)).

The creep specimens (length: 74 mm and diameter: 5 mm)

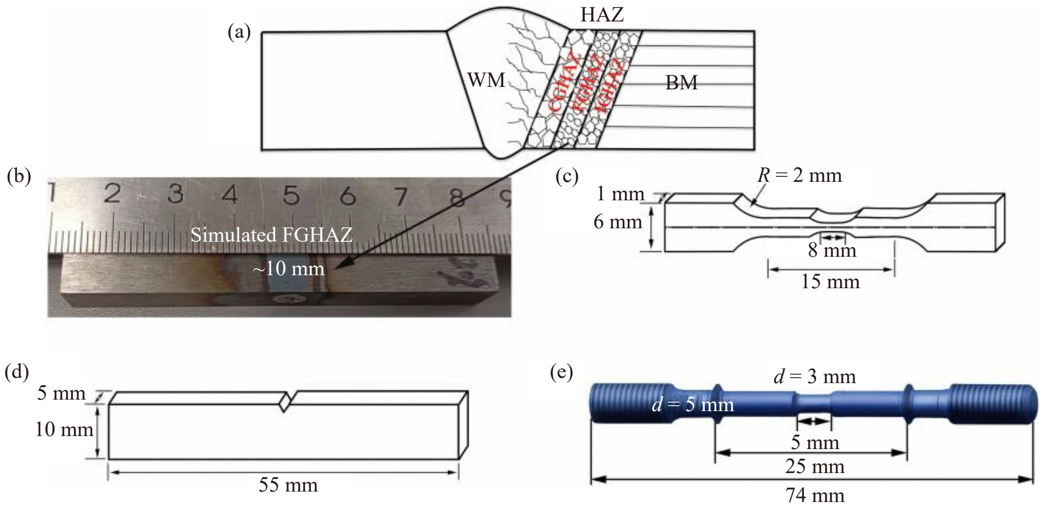

Fig. 2. (a) Location of FGHAZ in the weldments, (b) actual NT-FG and NCT-FG steels, (c) specially designed tensile specimens, (d) Charpy specimens, and (e) specially designed creep specimens.

were used in creep tests, which were carried out at 650°C under a uniaxial stress of 160 MPa. Meanwhile, a narrow portion with a diameter (*d*) of 3 mm and a length of 5 mm was machined within the FGHAZ (Fig. 2(e)). The test temperature was controlled within ±2°C, and the holding period prior to loading was approximately 30 min.

2.4. Microstructural characterization

Distribution analysis of $M_{23}C_6$ particles, creep damages, and fracture morphology was conducted through scanning electron microscopy (SEM, JSM-7800F). For SEM observation, the specimens were polished using a series of SiC papers up to 3000 grit, followed by mechanical polishing with 2.5 μm paste and etching in a mixed solution of $FeCl_3$ (5 g), HCl (15 mL), and H_2O (80 mL) at ambient temperature for 10 s. Electron backscattered diffraction (EBSD, JSM-7800F) was conducted to characterize the evolution of grain structure during the simulation and creep crack distribution. Before EBSD scanning, the specimens were mechanically polished with 0.25 μm paste and electrochemically polished using a solution of 20 mL $HClO_4$, 10 mL $C_3H_8O_3$, and 70 mL CH_3CH_2OH at a potential of 20 V for 15 s. Transmission electron microscopy (TEM, JEM-ARM200F) was performed to observe the precipitation of $M_{23}C_6$, MX, and Cu-rich phases and the evolution of laths and dislocations. For TEM observation, the specimens were first manually polished to 30 μm in thickness and twin-jet polished using a solution of 10 mL $HClO_4$ and 90 mL CH_3CH_2OH at −25°C. Electron microprobe analysis (EMPA) was conducted on the distributions of Cr and C. The specimens for EMPA were prepared following the procedure conducted for those used in SEM observations.

3. Results and discussion

3.1. Microstructural evolution

3.1.1. Initial structure of NT and NCT steels

Fig. 3 shows the initial microstructures of NT and NCT steels. The NT and NCT steel exhibited similar microstructural characteristics involving prior austenite grain boundaries (PAGs) that consisted of blocks (Fig. 3(a) and (d)). Dispersed $M_{23}C_6$ particles precipitated along the boundaries of PAGs, blocks, and laths in NT and NCT steels, and they could effectively impede the boundary migrations during aging or creep period [13,38]. The NCT steel had a relatively smaller average particle size (~70 nm) than the NT steel (~90 nm) (Fig. 3(b) and (e), respectively). Additionally, the NCT steel exhibited a finer lath structure due to rolling deformation. The NT and NCT steels had average lath widths of ~438.8 and ~398.7 nm, respectively (Fig. 3(c) and (f)). The dislocation structures of both steels can be observed in the forms of dislocation lines and tangles, and the NCT steel contained a higher proportion of dislocation tangles than the NT steel. For the latter, dislocation tangles were only introduced to the lath interior during the phase transformation between austenite and martensite to accommodate lattice mismatch [39]. By contrast, more complex dislocation tangles can be generated within the matrix of the NCT steel through the rolling process. X-ray diffraction with Cu-K_α radiation revealed dislocation densities of ~3.1×10^{14} and ~3.95×10^{14} m^{-2} for the NT and NCT steels, respectively (Fig. 3(c) and (f)).

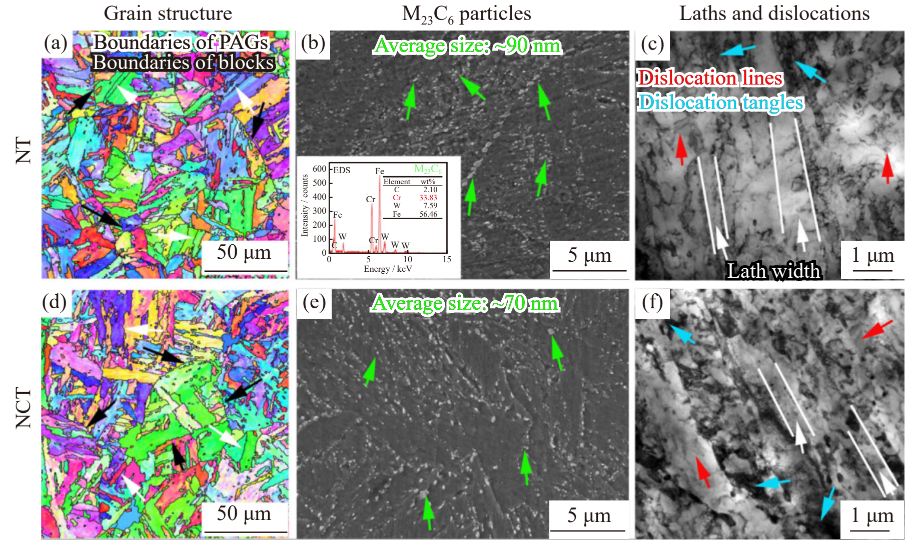

Fig. 3. Initial microstructures of the NT and NCT steels: (a, d) grain structure characterized by EBSD, (b, e) $M_{23}C_6$ particles observed via SEM, and (c, f) lath and dislocation structure displayed by TEM.

3.1.2. Grain structure and $M_{23}C_6$ particles of NT-FG and NCT-FG steels

Fig. 4 displays the grain structure, distribution of undissolved $M_{23}C_6$ particles, and distributions of C and Cr in the NT-FG and NCT-FG steels before PWHT. During thermal cycles at temperatures higher than the Ac_3, grain refinement usually occurs due to the diffusional reverse transformation of γ to α in traditional martensitic heat-resistant steels [40]. Only partial fine grains were formed in the NT-FG steel because of the higher B content of G115 steel (Fig. 4(a)), which

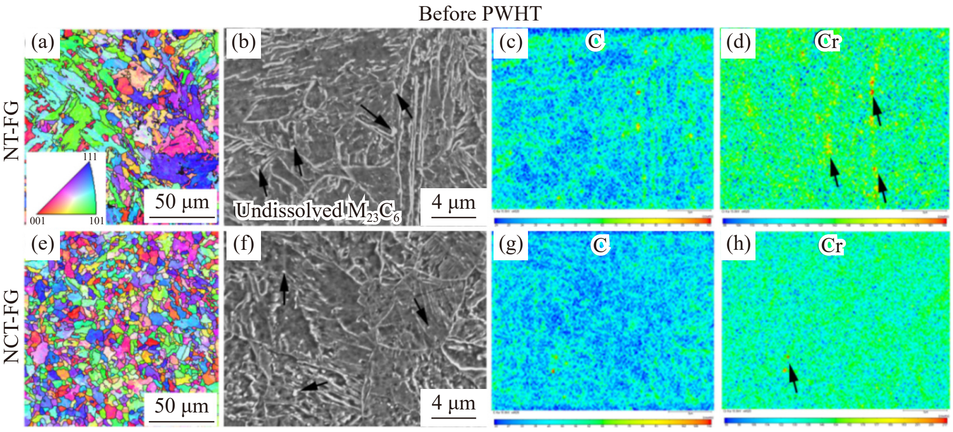

Fig. 4. Microstructure of the NT-FG and NCT-FG steels before PWHT: (a, e) grain structure characterized by EBSD, (b, f) undissolved $M_{23}C_6$ particles observed by SEM, and (c, d, g, h) distributions of C and Cr analyzed by EMPA.

can segregate at grain boundaries and reduce the boundary energy for γ/α transformation [41]. The pre-existing PAGs in the NCT-FG steel were uniformly refined during thermal cycling owing to the deformation-induced dislocations or defects with higher stored energy, which can provide additional energy for γ/α transformation (Figs. 4(e) and 3(f)). Despite the susceptibility of grain boundaries to crack propagation in the FGHAZ during creep period, Liu *et al.* [40] proved the insignificant effect of the fine-grain structure on creep strength during long-term creep, and the crucial factor was the scarce precipitation of $M_{23}C_6$ within the grain interior.

In the equilibrium state, $M_{23}C_6$ particles can be completely dissolved into the matrix at the Ac_3 temperature of the G115 steel [42]. However, some undissolved $M_{23}C_6$ particles can still be tracked in the NT-FG steel after thermal cycling at 1050°C (higher than Ac_3) owing to the transient holding period of 4 s (Fig. 4(b)). In the NCT-FG steel, although some undissolved $M_{23}C_6$ particles can also be observed, the size and number of residual particles have been evidently reduced (Fig. 4(f)). This can be explained from two aspects. One is that the size of pre-formed $M_{23}C_6$ particles during tempering in the NCT steel is relatively smaller than that in the NT steel (Fig. 3(b) and (e)), which is contributed to the dissolution process during thermal cycles. The other is that the deformation-induced dislocations connected with the $M_{23}C_6$ particles can accelerate the diffusion of particle forming elements toward the matrix (Fig. 3(f)).

In EMPA maps, the colors from blue to red represent the degrees of element accumulation from the minimum to the maximum, and the high-intensity spots of Cr or C indicate the undissolved $M_{23}C_6$ particles or segregation of atoms. For the NT-FG steel (Fig. 4(c) and (d)), these undissolved $M_{23}C_6$ particles were identified by the red points denoting the C- and Cr-enriched regions. In addition, Cr and C exhibited serious segregation at PAG and block boundaries after thermal cycling, which was harmful to the even reprecipitation of $M_{23}C_6$ particles during PWHT [17]. The density of undissolved $M_{23}C_6$ particles was reduced remarkably in the NCT-FG steel (Fig. 4(g) and (h)), and the segregation of C and Cr after thermal cycling was effectively relieved, which contributed to the dispersed reprecipitation of $M_{23}C_6$ particles within the newly formed PAGs.

Fig. 5 presents the grain structure and distribution of reprecipitated $M_{23}C_6$ particles in the NT-FG and NCT-FG steels after PWHT. Compared with that before PWHT, the evolution of PAGs in both steels was negligible after PWHT (Fig. 5(a) and (c)). The precipitation conditions of $M_{23}C_6$ particles in the two steels differed remarkably. In the NT-FG steel (Fig. 5(b)), in addition to the coarsening of undissolved $M_{23}C_6$ particles, only a few particles can re-precipitate at the sub-boundaries within the newly formed grains during PWHT due to the segregation of C and Cr elements, which seriously weakened the precipitate strengthening and boundary strengthening effects under creep exposure [40]. However, dispersed $M_{23}C_6$ particles precipitated within the matrix in the NCT-FG steel (Fig. 5(d)), including the boundaries of PAGs, blocks, and laths. Moreover, the NCT-FG steel had a smaller particle size and relatively higher density than the NT-FG steel. In detail, the NT-FG and NCT-FG steels had particle sizes of approximately 250 and 160 nm, respectively, and the densities were around 2.30 and 4.75 μm^{-2}.

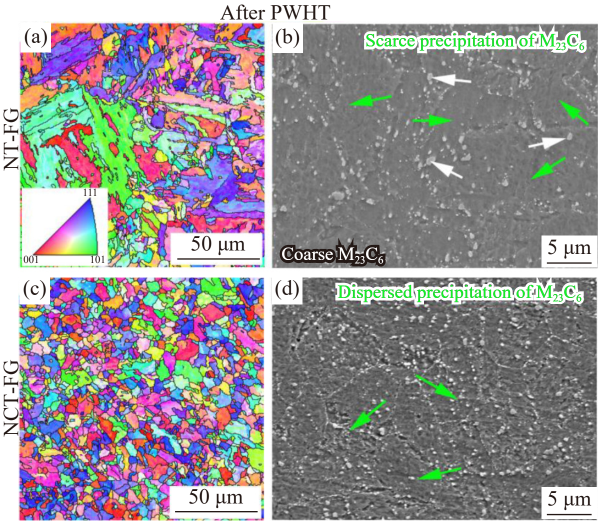

Fig. 5. Microstructures of NT-FG and NCT-FG steels after PWHT: (a, c) grain structures characterized through EBSD and (b, d) reprecipitated $M_{23}C_6$ particles observed via SEM.

In conclusion, the developed NCT treatment can be used to solve the issues involving element segregation and uneven distribution of $M_{23}C_6$ particles, which universally exist within the FGHAZ in martensitic heat-resistant steel weldments. Our previous investigation [2] has proven that during long-term creep of G115 steel weldments under 140 MPa, dispersed distribution of coarse $M_{23}C_6$ particles can be traced around the microcracks, which indicates that these particles were inducements of creep damages caused by unmatched deformation abilities. Liu *et al.* [40] proved that during creep of FGHAZ in Gr. 92 steel weldments, the boundaries without dispersed $M_{23}C_6$ particles were the favorable nucleation sites for creep voids. Moreover, Abe [43] reported that during creep period, $M_{23}C_6$ particles exhibited an important role on improving creep strength of 9%Cr tempered martensitic steels, due to their relatively higher density compared with other precipitates. Hence, the reduced size of $M_{23}C_6$ particles and their accelerated uniform precipitation along various boundaries during PWHT can effectively impede the formation of creep damages.

3.1.3. Laths, dislocations and nano-sized MX and Cu-rich particles in NT-FG and NCT-FG steels

Fig. 6(a) and (b) shows the lath and dislocation structures of the NT-FG and NCT-FG steels before PWHT. The NT-FG steel had a typical lath structure filled with complex dislocation structures that can provide lath strengthening and dislocation strengthening effects during creep [44–45]. The NCT-FG steel contained fresh triple boundaries of PAGs in addition to the fine lath structure with dislocation tangles. Fig. 6(c) and (d) displays the structural evolution of laths in the NT-FG and NCT-FG steels during PWHT. Most laths in the NT-FG steel transformed into sub-grains due to the limited precipitation of $M_{23}C_6$ particles along the fresh boundaries, which seriously weakened the ability for pinning boundaries. Moreover, the dislocation tangles exhibited evident recovery, which led to the formation of simple dislocation lines. By contrast, although the NCT steel also exhibited the formation of some subgrains, its lath characteristic still remained dominant. Additionally, the extent of dislocation recovery is relatively slight.

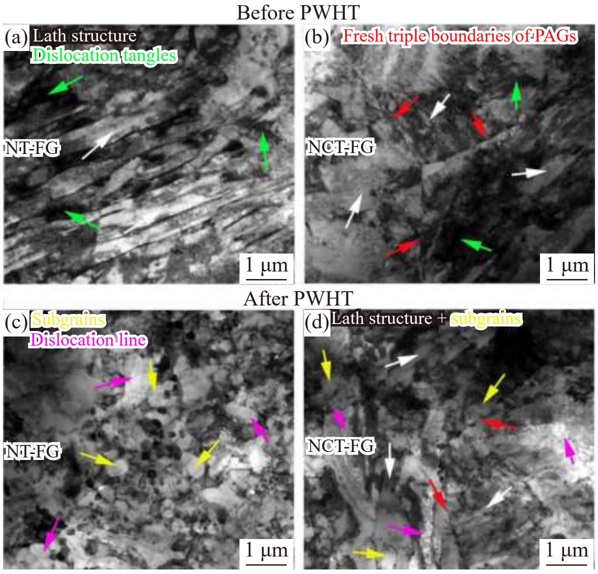

Fig. 6. Lath and dislocation structures of the NT-FG and NCT-FG steels (a, b) before PWHT and (c, d) after PWHT.

Fig. 7 exhibits the different precipitations of strengthening particles in the NT-FG and NCT-FG steels after PWHT. In the NT-FG steel, the $M_{23}C_6$ particles exhibited sparse ring-shape distribution, and no particles could be observed within the grain interior, which weakened their ability for obstructing the sub-boundary migration [46–47]. While, in the NCT-FG steel, most fine $M_{23}C_6$ particles dispersedly precipitated along the boundaries of PAGs and blocks. This is consistent with that characterized by SEM (Fig. 5). In addition to $M_{23}C_6$ particles, Cu-rich phases and MX particles also contributed to improve the creep resistance of G115 steel by impeding dislocation recovery [10,48]. The energy dispersive spectroscopy (EDS) maps of Cu and Nb revealed that compared with the NT-FG steel, the NCT-FG steel contained more Cu-rich phases and Nb-rich MX particles. This can be ascribed to the deformation-induced dislocations, which could provide additional nucleation sites [26,49]. In detail, the densities of Cu-rich phases in the NT-FG and NCT-FG steels were approximately 0.4 and 1.33 μm^{-2}, respectively, and those of MX particles were around 0.23 and 0.47 μm^{-2}.

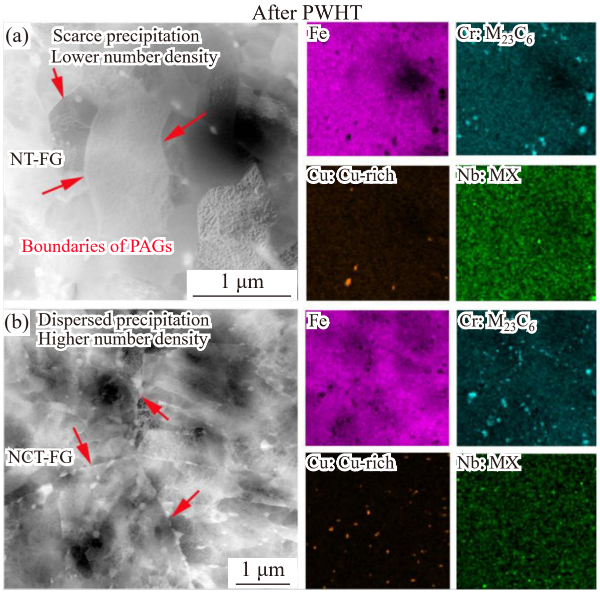

Fig. 7. Distribution of precipitates in the (a) NT-FG and (b) NCT-FG steels and the corresponding EDS maps of Fe, Cr, Cu, and Nb.

3.2. Mechanical properties

3.2.1. Tensile strength and Charpy impact toughness of NT-FG and NCT-FG steels

In addition to creep strength, satisfactory tensile strength and impact toughness also affect the safe operation of G115 steel. Fig. 8 displays the engineering stress–strain curves of the NT-FG and NCT-FG steels and their corresponding impact toughness. Before PWHT, a relatively higher ultimate tensile strength (~783.5 MPa) was observed in the NCT-FG

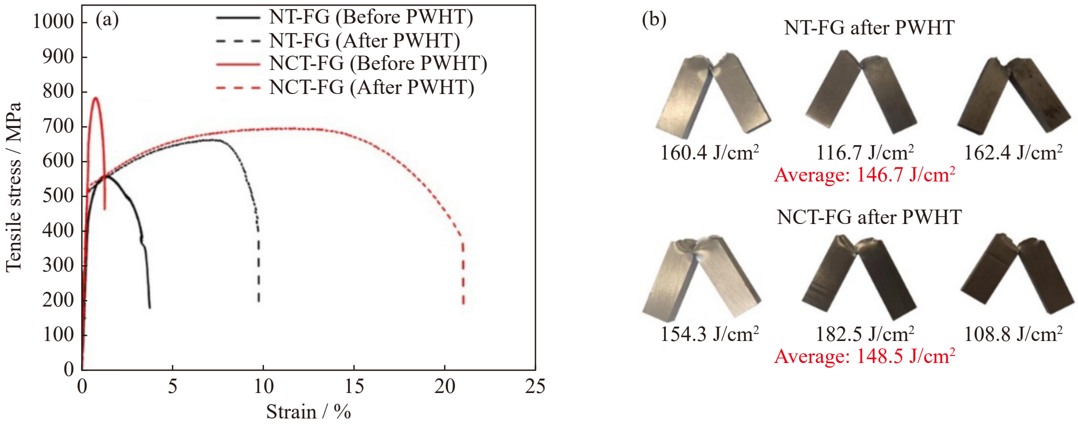

Fig. 8. (a) Engineering stress–strain curves obtained before and after PWHT and (b) impact toughness measured after PWHT of the NT-FG and NCT-FG steels.

steel compared with that in the NT-FG steel (~658.7 MPa) (solid lines in Fig. 8(a)). This can be attributed to the accelerated dissolution of $M_{23}C_6$ particles in the NCT-FG steel during thermal cycling (Fig. 4), which resulted in a higher content of solute Cr or C atoms within the matrix. In addition, the refined grains and narrow lath structure of the NCT-FG steel could provide more sub-boundaries in the unit area and higher dislocation density. During tensile deformation, the pinned force offered to sub-boundaries and dislocations by these solute atoms, which needed higher external stress to overcome, was enhanced considerably, displaying a higher yield strength.

After PWHT, the ultimate tensile strength of NCT-FG steel decreased to ~695.4 MPa, and that of NT-FG steel slightly increased to ~662.7 MPa (dashed lines in Fig. 8(a)). Compared with the NT-FG steel, NCT-FG steel exhibited a sharply decreased strength, and this result could be attributed to the sufficient reprecipitation of $M_{23}C_6$ particles and the recovery of lath and dislocation structures, which reduced the solution strengthening, lath, and dislocation strengthening effects (Fig. 5). As for the slightly enhanced strength of the NT-FG steel, it may be caused by that the increased precipitation strengthening effect originated from the dispersed particles had offset and exceeded the reduced strengthening actions originated from solution atoms, laths, and dislocations. Fig. 8(b) shows that after PWHT, the NT-FG and NCT-FG steels exhibited high average impact toughness values of 146.7 and 148.5 J/cm^2, respectively.

In conclusion, the NCT-FG steel displayed excellent tensile strength and impact toughness compared with the NT-FG steel and satisfied the minimum required strength (>480 MPa) and toughness (>40 J/cm^2) as proposed in the T/CISA 003-2017 specification for industrial G115 steel pipes.

3.2.2. Creep strength of NT-FG and NCT-FG steels

Fig. 9 displays the creep displacement versus time curves of the NT-FG and NCT-FG steels after PWHT. Compared with that of the NT-FG steel (1069.3 h), the creep rupture life of the NCT-FG steel was prolonged to 1268.4 h, and had been significantly prolonged by 18.6%. This verifies the strategy that the creep strength of FGHAZ of the G115 steel can be reinforced by the NCT treatments.

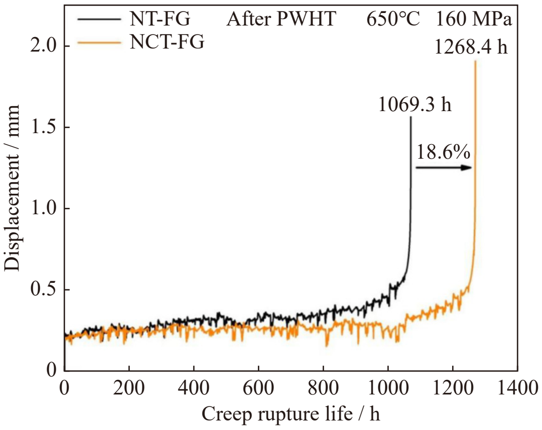

Fig. 9. Creep displacement versus time curves of the NT-FG and NCT-FG steels after PWHT.

The NCT process refined the $M_{23}C_6$ particles, which precipitated in the G115 steel during tempering and retained partial deformation-induced dislocations (Fig. 3). Thus, the dissolution of $M_{23}C_6$ particles into the matrix during thermal cycling could be accelerated in the FGHAZ, and the segregation of Cr and C along the boundaries of original PAGs and blocks was evidently relieved (Fig. 4). As a feedback, homogenized reprecipitation of fresh $M_{23}C_6$ particles within the newly formed reaustenitized grains occurred during PWHT, and it effectively obstructed boundary migrations during creep (Fig. 5). Moreover, compared with the NT-FG steel, the NCT-FG steel had a higher density of Cu- and Nb-rich particles, which could substantially impede dislocation movement and annihilation (Fig. 7). Hence, the improved creep resistance of the NCT-FG steel could be attributed to the reinforced interactions between nano-sized particles, dislocations, and boundaries.

3.2.3. Creep damages and fracture mechanism of NT-FG and NCT-FG steels

Fig. 10(a) and (b) presents the creep damages observed adjacent to the fracture frontier of the NT-FG and NCT-FG steels after creep rupture. Both steels contained creep damage in the form of microcavities and cracks, which were closely associated with cavity nucleation, growth, and coalescence. During creep, the motions of dislocations and boundaries were constantly impeded by coarse precipitates, around which stress concentration was generated, providing critical energy for the formation of microcavities. Then, the microcavities grew and connected with each other with further deformation, which led to microcrack formation. Finally, these microcracks were translated into a martensite fracture via boundary sliding and led to premature fracture [2,50].

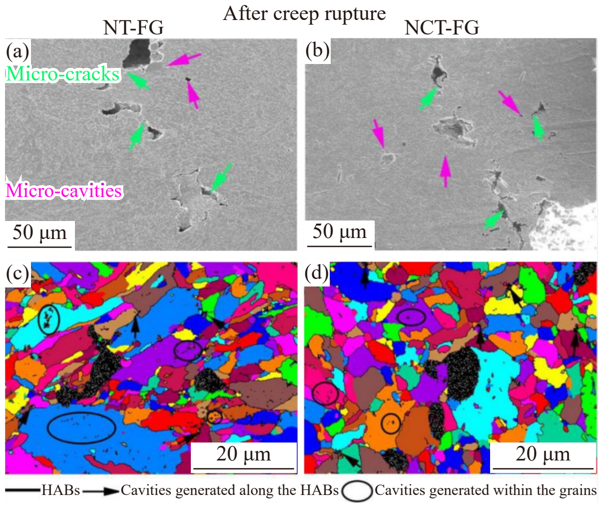

Fig. 10. Creep damages observed adjacent to the fracture frontier and the corresponding unique grain maps around microcracks in the (a, c) NT-FG and (b, d) NCT-FG steels after creep rupture.

To further clarify the formation location of creep cavities, Fig. 10(c) and (d) displays the unique grain maps observed around micro-cracks in the NT-FG and NCT-FG steels after creep rupture, and the different colors present different grains. In the NT-FG steel, in addition to the cavities that formed along the high-angle boundaries (HABs) of PAGs (shown by the black arrows), a substantial portion of cavities can be tracked within the grain interior (as indicated by the black ellipses). Meanwhile, in the NCT-FG steel, most cavities were generated along the HABs, and a few can be observed within the grains. In detail, the statistical densities of creep cavities along the HABs in the NT-FG and NCT-FG steels were approximately 0.032 and 0.011 μm^{-1}, respectively, and those within the grain interior were around 0.012 and 0.005 μm^{-2}. These results prove that compared with that of the NT-FG steel, the nucleation rate of creep cavities in the NCT-FG steel was effectively reduced.

To gain insights into the inducement of creep cavities, Fig. 11 presents the distribution of $M_{23}C_6$ particles and Laves phases around the microcavities of the NT-FG and NCT-FG steels after creep rupture. As displayed in the SEM images, the precipitates with gray color were mixtures of $M_{23}C_6$ particles and Laves phases, and in the back-scattered electron images, the white-bright particles were the single Laves phases due to the high atomic weight of W [9]. The comparison of Fig. 11(a) and (b) revealed the relatively larger $M_{23}C_6$ particles of the NT-FG steel compared with those of the NCT-FG steels. In addition, in both steels, coarse $M_{23}C_6$ particles could be tracked around the microcavities. Fig. 11(c) and (d) shows that dispersed Laves phases precipitated within the matrix during creep. These Laves phases constantly cause harm to the creep strength of ferrite/martensite steels during long-term creep due to their fast coarsening rate and high hardness [51–52]. However, evident accumulation of coarse Laves phases was not observed around creep cavities. These results suggest that compared with the Laves phases, coarse $M_{23}C_6$ particles should dominantly be responsible for the formation of creep damages in both steels.

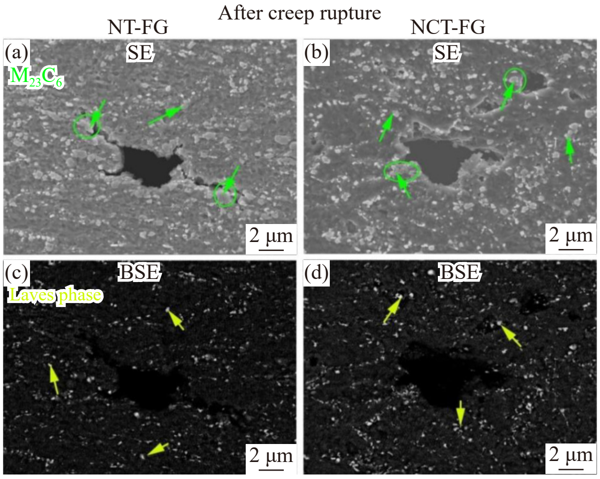

Fig. 11. Distribution of $M_{23}C_6$ particles and Laves phases observed around microcavities in the (a, c) NT-FG and (b, d) NCT-FG steels after creep rupture.

After synthetically considering Figs. 10 and 11, Fig. 12 schematically determines the formation forms of creep cavities in the NT-FG and NCT-FG steels after creep rupture. Creep cavities in the NT-FG steel existed in two forms: one is within the grain interior, and another is along the HABs decorated with coarse $M_{23}C_6$ particles. The creep cavities within the grain interior formed due to the lacking precipitation of $M_{23}C_6$ particles during PWHT as a result of the segregation of Cr or C during thermal cycling (Figs. 4 and 5), which weakened the sub-boundary strengthening effect. Meanwhile, the cavities along the HABs formed due to the coarse $M_{23}C_6$ particles, which evolved from their undissolved counterparts during thermal cycling and exhibited incompatible deformation with the adjacent matrix. Meanwhile, the NCT-FG steel contained only a few cavities within its grains due to the dispersed reprecipitation of $M_{23}C_6$ particles during PWHT (Figs. 5 and 7). In addition, most cavities were generated along the HABs due to the presence of coarse $M_{23}C_6$ particles.

Fig. 13 displays the creep fracture morphologies of the NT-FG and NCT-FG steels after creep rupture. Both steels had a fracture surface with a cup-like feature, which is consisted of a shear-lip zone at the outer periphery and a fiber zone in the central region (Fig. 13(a) and (d)). Fracture analysis revealed a higher fracture shrinkage ratio of the NT-FG steel (~67.1%) than that of the NCT-FG steel (~51.5%). The shear-lip and central fiber zones of the NT-FG steel featured some small and shallow dimples combined with large and deep dimples (Fig. 13(b) and (c)), suggesting ductility failure. The shear-lip zone of the NCT-FG steel contained some

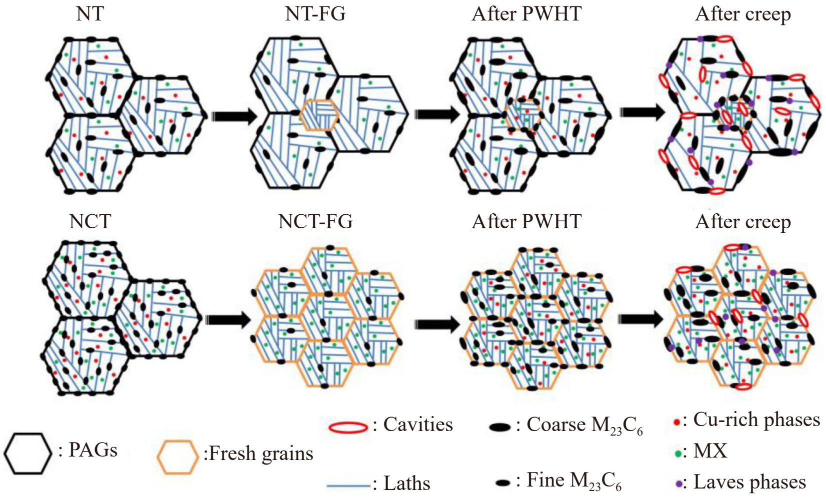

Fig. 12. Formation forms of creep cavities in the NT-FG and NCT-FG steels after creep rupture: within the grain interior without $M_{23}C_6$ particles and along the HABs decorated with coarse $M_{23}C_6$ particles.

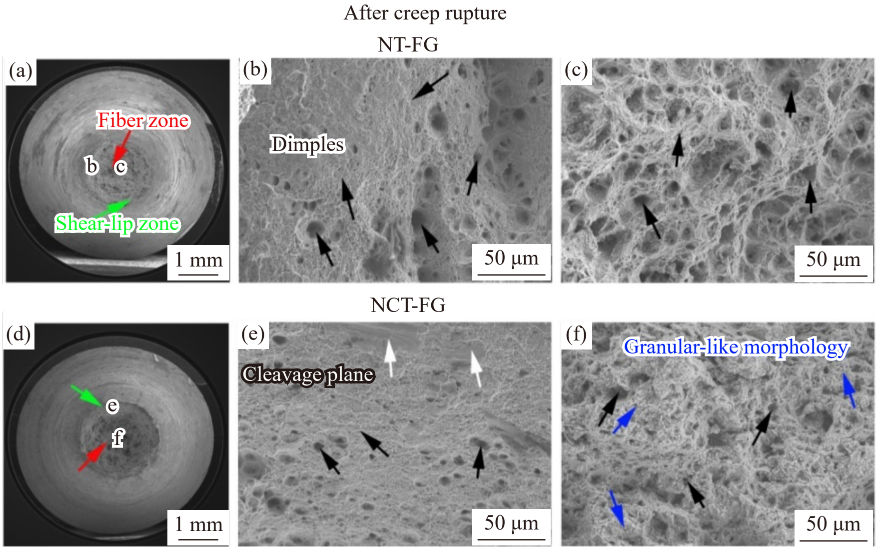

Fig. 13. Creep fracture morphology of the (a–c) NT-FG and (d–f) NCT-FG steels after creep rupture.

cleavage planes in addition to the dimple structure. Moreover, a granular-like morphology formed in the fiber zone (Fig. 13(e) and (f)), which indicates that the fracture of the NCT-FG steel occurred in the combined mode of ductility and brittleness.

4. Conclusions

A newly designed NCT process was successfully developed to improve the creep strength of the FGHAZ in G115 steel weldments. The microstructural evolution, mechanical properties, and creep strength of the NT-FG and NCT-FG steels were systematically investigated, and the following conclusions were drawn:

(1) The NCT treatment can reduce the size of $M_{23}C_6$ particles and refine the lath structure of G115 steel after tempering. Moreover, deformation-induced dislocations were partially retained.

(2) Compared with that in the NT-FG steel, the dissolution of $M_{23}C_6$ particles was accelerated, and the segregation of Cr and C was relieved in the NCT-FG steel, contributing to the dispersed reprecipitation of fresh $M_{23}C_6$ particles. In addition, the precipitation of MX and Cu-rich phases within the lath interior was evidently promoted.

(3) The NCT-FG steel exhibited excellent tensile strength and impact toughness compared with the NT-FG steel. Moreover, the NCT-FG steel presented a considerably improved creep strength, which can be attributed to the reinforced interactions among precipitates, dislocations, and boundaries.

(4) The NT-FG steel contained creep cavities that formed along the HABs of PAGs or blocks and within the grain interior. Meanwhile, most creep cavities in the NCT-FG steel were generated along the HABs, and the corresponding nucleation rate of creep cavities was effectively reduced.

Acknowledgements

This work was financially supported by the National Key R&D Program of China (No. 2022YFB3705300), the National Natural Science Foundation of China (Nos. U1960204 and 51974199), and the Postdoctoral Fellowship Program of CPSF (No. GZB20230515).

Conflict of Interest

Yongchang Liu is an editorial board member for this journal and was not involved in the editorial review or the decision to publish this article. The authors declare that they have no known competing financial interests or personal relationships that could have appeared to influence the work reported in this paper.

References

[1] G. Dak and C. Pandey, A critical review on dissimilar welds joint between martensitic and austenitic steel for power plant application, *J. Manuf. Process.*, 58(2020), p. 377.

[2] J.W. Zhang, L.M. Yu, Q.Z. Gao, *et al*., Creep behavior, microstructure evolution and fracture mechanism of a novel martensite heat resistance steel G115 affected by prior cold deformation, *Mater. Sci. Eng. A*, 850(2022), art. No. 143564.

[3] H.S. He, L.M. Yu, C.X. Liu, H.J. Li, Q.Z. Gao, and Y.C. Liu, Research progress of a novel martensitic heat-resistant steel G115, *Acta Metall. Sin.*, 58(2022), No. 3, p. 311.

[4] L.Q. Xu, D.T. Zhang, Y.C. Liu, *et al*., Precipitation behavior and martensite lath coarsening during tempering of T/P92 ferritic heat-resistant steel, *Int. J. Miner. Metall. Mater.*, 21(2014), No. 5, p. 438.

[5] J.H. Zhou, Y.F. Shen, and N. Jia, Strengthening mechanisms of reduced activation ferritic/martensitic steels: A review, *Int. J. Miner. Metall. Mater.*, 28(2021), No. 3, p. 335.

[6] Q.Z. Gao, Z. Yuan, Q.S. Ma, L.M. Yu, and H.J. Li, Strengthening and toughening optimizations of novel G115 martensitic steel: Utilizing secondary normalizing process, *Mater. Sci. Eng. A*, 852(2022), art. No. 143621.

[7] H.S. He, J.W. Zhang, L.M. Yu, *et al*., Effects of Cu-rich phases on microstructure evolution and creep deformation behavior of a novel martensitic heat-resistant steel G115, *Mater. Sci. Eng. A*, 855(2022), art. No. 143937.

[8] Z. Liu, Z.D. Liu, X.T. Wang, and Z.Z. Chen, Investigation of the microstructure and strength in G115 steel with the different concentration of tungsten during creep test, *Mater. Charact.*, 149(2019), p. 95.

[9] Z. Liu, X.T. Wang, and C. Dong, Effect of boron on G115 martensitic heat resistant steel during aging at 650°C, *Mater. Sci. Eng. A*, 787(2020), art. No. 139529.

[10] B. Xiao, L.Y. Xu, C. Cayron, J. Xue, G. Sha, and R. Logé, Solute-dislocation interactions and creep-enhanced Cu precipitation in a novel ferritic-martensitic steel, *Acta Mater.*, 195(2020), p. 199.

[11] Z. Liu, Z.D. Liu, X.T. Wang, Z.Z. Chen, and L.T. Ma, Evolution of the microstructure in aged G115 steels with the different concentration of tungsten, *Mater. Sci. Eng. A*, 729(2018), p. 161.

[12] Z. Liu, Z.D. Liu, X.T. Wang, C. Dong, Z.Z. Chen, and H.S. Bao, The microstructural evolution and mechanical property in G115 steels during long-term aging at 650°C, *Mater. Res. Express*, 6(2019), No. 11, art. No. 116527.

[13] Y.H. Yu, Z.D. Liu, C. Zhang, *et al*., Correlation of creep fracture lifetime with microstructure evolution and cavity behaviors in G115 martensitic heat-resistant steel, *Mater. Sci. Eng. A*, 788(2020), art. No. 139468.

[14] Z.W. Wang, M. Zhang, C. Li, *et al*., Achieving a high-strength dissimilar joint of T91 heat-resistant steel to 316L stainless steel via friction stir welding, *Int. J. Miner. Metall. Mater.*, 30(2023), No. 1, p. 166.

[15] J.W. Zhang, L.M. Yu, R. Ding, *et al*., Deformation behavior, microstructure evolution, and rupture mechanism of the novel G115 steel welded joint during creep, *Mater. Charact.*, 205(2023), art. No. 113275.

[16] C. Pandey, M.M. Mahapatra, and P. Kumar, Effect of post weld heat treatments on fracture frontier and type IV cracking nature of the crept P91 welded sample, *Mater. Sci. Eng. A*, 731(2018), p. 249.

[17] Y.Y. Wang, R. Kannan, and L.J. Li, Correlation between intercritical heat-affected zone and type IV creep damage zone in grade 91 steel, *Metall. Mater. Trans. A*, 49(2018), No. 4, p. 1264.

[18] J.W. Zhang, L.M. Yu, Q.Z. Gao, *et al*., A new strategy to improve the creep strength of a novel G115 steel by accelerating the precipitation of nano-sized MX and Cu-rich particles, *Scripta Mater.*, 220(2022), art. No. 114903.

[19] J. Hoffmann, M. Rieth, M. Klimenkov, and S. Baumgärtner, Improvement of EUROFER's mechanical properties by optimized chemical compositions and thermo-mechanical treatments, *Nucl. Mater. Energy*, 16(2018), p. 88.

[20] S. Hollner, B. Fournier, J. Le Pendu, *et al*., High-temperature mechanical properties improvement on modified 9Cr–1Mo martensitic steel through thermomechanical treatments, *J. Nucl. Mater.*, 405(2010), No. 2, p. 101.

[21] R.L. Klueh, N. Hashimoto, and P.J. Maziasz, New nano-particle-strengthened ferritic/martensitic steels by conventional thermo-mechanical treatment, *J. Nucl. Mater.*, 367-370(2007), p. 48.

[22] T. Sakthivel, P. Shruti, P. Parameswaran, G.V.S.N. Rao, K. Laha, and T.S. Rao, Enhancement in creep strength of modified 9CR–1MO steel through thermo-mechanical treatment, *Trans. Indian Inst. Met.*, 70(2017), No. 5, p. 1177.

[23] J. Vivas, C. Capdevila, E. Altstadt, M. Houska, and D. San-Martín, Importance of austenitization temperature and ausforming on creep strength in 9Cr ferritic/martensitic steel, *Scripta Mater.*, 153(2018), p. 14.

[24] T. Sakthivel, S.M. Nandeswarudu, P. Shruti, *et al*., An improvement in creep strength of thermo-mechanical treated modified 9Cr–1Mo steel weld joint, *Mater. High Temp.*, 36(2019), No. 1, p. 76.

[25] P. Prakash, J. Vanaja, N. Srinivasan, P. Parameswaran, G.V.S.N. Rao, and K. Laha, Effect of thermo-mechanical treatment on tensile properties of reduced activation ferritic-martensitic steel, *Mater. Sci. Eng. A*, 724(2018), p. 171.

[26] M. Nöhrer, W. Mayer, S. Primig, S. Zamberger, E. Kozeschnik, and H. Leitner, Influence of deformation on the precipitation behavior of Nb(CN) in austenite and ferrite, *Metall. Mater. Trans. A*, 45(2014), No. 10, p. 4210.

[27] P. Prakash, J. Vanaja, G.V P. Reddy, K. Laha, and G.V.S N. Rao, On the effect of thermo-mechanical treatment on creep deformation and rupture behaviour of a reduced activation ferritic-martensitic steel, *J. Nucl. Mater.*, 520(2019), p. 65.

[28] B.A. Shassere, Y. Yamamoto, and S.S. Babu, Toward improving the type IV cracking resistance in Cr–Mo steel weld through thermo-mechanical processing, *Metall. Mater. Trans. A*, 47(2016), No. 5, p. 2188.

[29] P. Yan, Z.D. Liu, H.S. Bao, Y.Q. Weng, and W. Liu, Effect of normalizing temperature on the strength of 9Cr–3W–3Co martensitic heat resistant steel, *Mater. Sci. Eng. A*, 597(2014), p. 148.

[30] P. Yan, Z.D. Liu, H.S. Bao, Y.Q. Weng, and W. Liu, Effect of tempering temperature on the toughness of 9Cr–3W–3Co martensitic heat resistant steel, *Mater. Des.*, 54(2014), p. 874.

[31] J.W. Zhang, L.M. Yu, Q.Z. Gao, *et al*., Development of weld

filler material to match the advanced martensitic heat resistance steel G115 and tailoring the performance by tempering temperature, *J. Mater. Res. Technol.*, 21(2022), p. 2515.

[32] J. Vivas, C. Capdevila, E. Altstadt, M. Houska, I. Sabirov, and D. San-Martín, Microstructural degradation and creep fracture behavior of conventionally and thermomechanically treated 9% chromium heat resistant steel, *Met. Mater. Int.*, 25(2019), No. 2, p. 343.

[33] A. Khajuria, M. Akhtar, R. Bedi, *et al.*, Microstructural investigations on simulated intercritical heat-affected zone of boron modified P91-steel, *Mater. Sci. Technol.*, 36(2020), No. 13, p. 1407.

[34] M. Dunđer, T. Vuherer, I. Samardžić, and D. Marić, Analysis of heat-affected zone microstructures of steel P92 after welding and after post-weld heat treatment, *Int. J. Adv. Manuf. Technol.*, 102(2019), No. 9-12, p. 3801.

[35] A. Khajuria, M. Akhtar, R. Bedi, *et al.*, Influence of boron on microstructure and mechanical properties of Gleeble simulated heat-affected zone in P91 steel, *Int. J. Press. Vessels Pip.*, 188(2020), art. No. 104246.

[36] C. Pandey, M.M. Mahapatra, P. Kumar, J.G. Thakre, and N. Saini, Role of evolving microstructure on the mechanical behaviour of P92 steel welded joint in as-welded and post weld heat treated state, *J. Mater. Process. Technol.*, 263(2019), p. 241.

[37] H.Y. Azad, S.H.M. Anijdan, and H. Najafi, The effect of PWHT on the microstructural evolution, carbides formation and mechanical properties of a Nb containing martensitic heat resistance steel used in gas turbine, *Mater. Sci. Eng. A*, 793(2020), art. No. 139810.

[38] Z. Liu, Z.D. Liu, Z.Z. Chen, X.T. Wang, H.S. Bao, and C. Dong, Microstructure and creep strength evolution in G115 steel during creep at 650°C, *Mater. Res. Express*, 7(2020), No. 1, art. No. 016528.

[39] Q.Z. Gao, C. Wang, F. Qu, Y.L. Wang, and Z.X. Qiao, Martensite transformation kinetics in 9Cr–1.7W–0.4Mo–Co ferritic steel, *J. Alloys Compd.*, 610(2014), p. 322.

[40] Y. Liu, S. Tsukamoto, T. Shirane, and F. Abe, Formation mechanism of type IV failure in high Cr ferritic heat-resistant steel-welded joint, *Metall. Mater. Trans. A*, 44(2013), No. 10, p. 4626.

[41] T. Matsunaga, H. Hongo, M. Tabuchi, and R. Sahara, Suppression of grain refinement in heat-affected zone of 9Cr–3W–3Co–VNb steels, *Mater. Sci. Eng. A*, 655(2016), p. 168.

[42] Y. Liang, W. Yan, X.B. Shi, *et al.*, On Laves phase in a 9Cr3W3CoB martensitic heat resistant steel when aged at high temperatures, *J. Mater. Sci. Technol.*, 85(2021), p. 129.

[43] F. Abe, Precipitate design for creep strengthening of 9% Cr tempered martensitic steel for ultra-supercritical power plants, *Sci. Technol. Adv. Mater.*, 9(2008), No. 1, art. No. 013002.

[44] F. Abe, New martensitic steels, [in] A.D. Gianfrancesco, ed., *Materials for Ultra-Supercritical and Advanced Ultra-Supercritical Power Plants*, Woodhead Publishing, Cambridge, 2017, p. 323.

[45] F. Abe, M. Igarashi, S. Wanikawa, *et al.*, Ultra steel project for advanced ferritic steels for 650°C USC boilers, [in] P. Neumann, D. Allen, and E. Teuckhoff, eds., *Steels and Materials for Power Plants*, Wiley-VCH Verlag GmbH, Weinheim, 2000, p. 299.

[46] Y.K. Wang, Q.S. Ma, Q.Z. Gao, *et al.*, Precipitation and strengthening behavior of M23C6 carbides in tempered G115 steel, *JOM*, 74(2022), No. 12, p. 4755.

[47] H. Wang, W. Yan, S. van Zwaag, *et al.*, On the 650°C thermostability of 9–12Cr heat resistant steels containing different precipitates, *Acta Mater.*, 134(2017), p. 143.

[48] J. Vivas, D. De-Castro, E. Altstadt, M. Houska, D. San-Martín, and C. Capdevila, Design and high temperature behavior of novel heat resistant steels strengthened by high density of stable nanoprecipitates, *Mater. Sci. Eng. A*, 793(2020), art. No. 139799.

[49] J. Vivas, C. Capdevila, E. Altstadt, *et al.*, Effect of ausforming temperature on creep strength of G91 investigated by means of small punch creep tests, *Mater. Sci. Eng. A*, 728(2018), p. 259.

[50] A. Benaarbia, X. Xu, W. Sun, A.A. Becker, and M.A.E. Jepson, Investigation of short-term creep deformation mechanisms in MarBN steel at elevated temperatures, *Mater. Sci. Eng. A*, 734(2018), p. 491.

[51] A. Kipelova, A. Belyakov, and R. Kaibyshev, Laves phase evolution in a modified P911 heat resistant steel during creep at 923 K, *Mater. Sci. Eng. A*, 532(2012), p. 71.

[52] O. Prat, J. Garcia, D. Rojas, C. Carrasco, and G. Inden, Investigations on the growth kinetics of Laves phase precipitates in 12% Cr creep-resistant steels: Experimental and DICTRA calculations, *Acta Mater.*, 58(2010), No. 18, p. 6142.